Accepted Manuscript

Cutting forces in fast-/slow tool servo diamond turning of micro-structured surfaces

Zhiwei Zhu, Suet To, Wu-Le Zhu, Peng Huang, Xiaoqin Zhou

PII: S0890-6955(18)30561-3
DOI: 10.1016/j.ijmachtools.2018.09.003
Reference: MTM 3372

To appear in: *International Journal of Machine Tools and Manufacture*

Received Date: 13 February 2018
Revised Date: 10 September 2018
Accepted Date: 16 September 2018

Please cite this article as: Z. Zhu, S. To, W.-L. Zhu, P. Huang, X. Zhou, Cutting forces in fast-/slow tool servo diamond turning of micro-structured surfaces, *International Journal of Machine Tools and Manufacture* (2018), doi: https://doi.org/10.1016/j.ijmachtools.2018.09.003.

Cutting forces in fast-/slow tool servo diamond turning of micro-structured surfaces

Zhiwei Zhu[a], Suet To[b], Wu-Le Zhu[c], Peng Huang[d], Xiaoqin Zhou[e]

[a] *School of Mechanical Engineering, Nanjing University of Science and Technology, Nanjing, J.S. 210094, China*
[b] *State Key Laboratory of Ultra-precision Machining Technology, Department of Industrial and Systems Engineering, The Hong Kong Polytechnic University, Kowloon, Hong Kong SAR, China*
[c] *Department of Micro-Engineering, Kyoto University, Nishikyo-ku, Kyoto, 615-8540, Japan*
[d] *College of Mechatronics and Control Engineering, Shenzhen University, Shenzhen, G.D. 518060, China*
[e] *School of Mechanical Science and Engineering, Jilin University, Changchun, J.L. 130022, China*

Preprint submitted to International Journal of Machine Tools and Manufacture *February 13, 2018*

Highlights

1 Systematic study of cutting forces in F-/STS is conducted both theoretically and experimentally;

2 A finite element model is developed to investigate plastic flow in deformation zones in F-/STS turning;

3 Material removal in F-/STS is highly dependent on the oscillated servo motion;

4 A mechanistic cutting force model considering both shearing and ploughing is developed;

5 The developed model is capable of capturing the time-varying cutting forces in F-/STS.

Cutting forces in fast-/slow tool servo diamond turning of micro-structured surfaces

---

Abstract

Although fast-/slow tool servo (F-/STS) diamond turning is widely employed to generate micro-structured surfaces, very limited attention has been focused on the cutting force which directly reflects the material removal behavior in F-/STS. In this study, theoretical analysis on the cutting force is conducted through both finite element and mechanistic analytical models to present a systematic investigation. Based on direct observation from the FE model that the shear angle varies with respect to the auxiliary servo motion, an analytical model is proposed to simultaneously predict the average and variation of the shear angle considering features of the oscillated servo motion. A comprehensive force model is developed for orthogonal cutting with a round-edged cutter, and the depth-of-cut (DoC) dependent shearing and ploughing effects are considered. With the shearing based material removal, dynamic shear strain, shear strain rate, and stress distribution inside the shear band are modeled together with the dynamic equivalent rake angle to derive the material removal force through the slip-line field theory, and the complex interaction between the chip and cutter in the rake face is also investigated to obtain the corresponding frictional force. With the DoC being smaller than the critical chip thickness, the ploughing force is modeled to be proportionate to the interference volume between the cutter and workpiece with full consideration of the dynamic equivalent clearance angle. Finally, the overall cutting force in F-/STS is estimated using the cutter edge discretization method with further experimental demonstration through the slow tool servo diamond turning of a typical micro-structured surface.

Keywords: Diamond turning, Fast-/slow tool servo, Micro-structured surface, Cutting force, Mechanistic model

---

Preprint submitted to International Journal of Machine Tools and Manufacture *September 17, 2018*

Nomenclature

$o_\mathrm{t}-x_\mathrm{t}z_\mathrm{t}$	Local coordinate system of the cutter
α_ro	Nominal rake angle
α_rv	Rake angle variation induced by servo motion
ϕ_o	Angle between shear plane and hornzontal plane
ζ	Ratio of the DoC to chip thickness
ζ_1, ζ_2	Equivalent ratio
v_z, v_0	Harmonic and horinontal cutting velocity in FE model
α_0	Included angle between $\overrightarrow{o_{k-1,l}o_{k,l}}$ and $o_\mathrm{t}x_\mathrm{t}$ axis
α_1	Included angle between $\overrightarrow{o_{k-1,l}D_1}$ and $\overrightarrow{o_{k,l}D_1}$
α_r	Practical rake angle
χ	Specific heat of the workpiece material
δ	The distance from the lowest point on the edge to the equivalent rake face
$\dot{z}_\mathrm{s}(i)$	Local slope of the desired surface
ϵ, $\dot{\epsilon_\mathrm{s}}$, $\dot{\epsilon}_0$	Equivalent strain, strain rate, and reference strain rate
η	Heat loss proportion
γ_s, $\dot{\gamma_\mathrm{s}}$	Shear strain, shear strain rate
κ	Practical clearance angle of the cutter
κ_o	Nominal clearance angle of the cutter
μ_e	Friction coefficient
μ_p	Friction coefficient for the ploughing
ϕ	Shear angle
ϕ_m	Shear angle variation induced by the z_m-axial servo motion
ϕ_s	Shear angle variation induced by the surface profile
	Equivalent contact angle
ρ	Density of the workpiece material
ρ, ϖ, z_m	Cylindrical coordinates of the machine tool
ρ_max	Radius of the workpiece
$\rho_{k,l}$, $\varpi_{k,l}$	Polar and angular axis of point $o_{k,l}$

σ_{n}	Normal stress on the rake face of the cutter
σ_{s1}	Stress at the free surface in the shear band
σ_{s2}	Stress at the bottom end in the shear band
τ_{st}	Shear stress at the sticking region
θ_i	Relative angle between the i-th cutting piece and the $o_{\mathrm{t}}z_{\mathrm{t}}$ axis
$\varLambda_{k,l}^{(i)}$	Width for the i-th cutting piece at point $o_{k,l}$
ϱ	Angular position for critical chip thickness
ξ	Multiple factor
a	Constant relating the distribution
A, B, C, m, n	Parameters of the Johnson-Cook model
C_{ox}	Shear strain rate factor
$d_{k,l}$	Distance between $o_{k-1,l}$ and $o_{k,l}$
$F_{\mathrm{c,p}}(i)$	Radial ploughing force for the i-th cutting piece
$F_{\mathrm{c}}(i)$	Main cutting force for the i-th cutting piece
$F_{\mathrm{n}}(i),\ F_{\mathrm{f}}(i)$	Normal and frictional force on the cutter for the i-th cutting piece
f_{s}	Feedrate per revolution
$F_{\mathrm{t,p}}(i)$	Frictional ploughing force for the i-th cutting piece
$F_{\mathrm{t}}(i)$	Thrust force for the i-th cutting piece
h_{o}	z_{t}-axial coordinate of the free surface
h_{s}	Critical chip thickness
$h_{k,l}^{(i)}$	Practical DoC for the i-th cutting piece at point $o_{k,l}$
$h_{k,l}^{(i)}$	The practical DoC for the i-th ctting piece
k_{int}	Proportion ratio relating the interfrence volume and force
$k_{\mathrm{n}},\ k_{\mathrm{f}}$	Equivalent proportionality factor for the normal and frictional forces
l_{ct}	Contact length between the tool and cutter
l_{st}	Sticking length of the chip on the rake face
l_{s}	Length of the shear band
N	Angular sampling ratio for one revolution
n	Rotational speed of the spindle

N_t	Descritization ratio of the cutting region
$o-uw$	Local Cartesian coordinate system fixed at the shear band
$o_\mathrm{m}-x_\mathrm{m}y_\mathrm{m}z_\mathrm{m}$	Cartesian coordinate system of the machine tool
$o_{k,l}$	The l-th cutter location point in the k-th revolution
r_e	Edge radius
R_t	Nose radius of the cutter
s	Distance to the lowest point at the tool edge
$S(\cdot)$	Function of the desired surface
$S_\mathrm{p}(i)$	Interference area between the cutter and workpiece during ploughing
$T_0,\ T_\mathrm{m},\ T_\mathrm{s}$	room temperature, melting temperature, working temperature
$v_\perp$	Velocity vertical to the shear band
v_s	Velocity along the shear band
$v_{k,l}$	Cutting velocity at point $o_{k,l}$
$v_{k,l}^{(\mathrm{c})}$	Cutting velocity component induced by spindle rotation at point $o_{k,l}$
$x_\mathrm{a},\ z_\mathrm{a}$	Coordinates of point A
$x_\mathrm{b},\ z_\mathrm{b}$	Coordinates of point B
$x_\mathrm{c},\ z_\mathrm{c}$	Coordinates of point C
z_0	Pre-set virtual position
z_s	z_m-axial coordinate of the desired surface in $o_\mathrm{m}-x_\mathrm{m}y_\mathrm{m}z_\mathrm{m}$
$z_{k,l}^{(\mathrm{s})}$	z_m-axial coordinate of the projected tool edge on the desired surface
$z_{k,l}^{(\mathrm{t})}$	z_m-axial coordinates of the cutter edge at point $o_{\{}k,l\}$
$v_{k,l}^{(\mathrm{m})}$	Servo velocity along the z_m-axis at point $o_{k,l}$

1. Introduction

As a very promising technique, fast-/slow tool servo (F-/STS) diamond turning has been widely applied for the generation of micro-structured functional surfaces in recent years. In essential, fast and slow tool servos have the same cutting kinematics featuring an oscillated servo motion along the spindle axis synthesized by the spindle rotation. During cutting, the workpiece rotates with the spindle, and the diamond cutter precisely follows the required time-varying trajectory to generate the desired micro-structured surfaces. With the last three decades, a large amount of efforts have been devoted to the improvement of F-/STS, including mechatronic system development [1], toolpath optimization [2, 3], machining accuracy improvement [4], and machining capability extension for different materials [5] as well as for different shapes [6, 7].

Cutting force is an important physical quantity for F-/STS which reflects the direct reaction between the cutter and workpiece. Taking advantage of the rich information involved in the cutting force which is resulted from the whole cutting loop, the force controlled tool servo is demonstrated to be very promising for the generation of complicated surfaces, with the capability to be insensitive to changes of the working conditions. For instance, taking advantage of constant force control through the force sensing integrated F-/STS, grooves with constant depth can be generated on curved surfaces without prior-knowledge of the surface shapes to be grooved [8, 9]. To improve the machining accuracy, a constant cutting force based turning of a micro-structured surface is performed through a double axial FTS [10]. Generally speaking, prediction of the required cutting forces in advance is the base to achieve the force-controlled F-/STS. However, with the current force controlled cutting, a calibration between the depth-of-cut (DoC) and cutting force is firstly conducted with the assumption that the required force is linearly dependent on the material removal area during the whole process [8–10]. To better predict the cutting force for the generation of a complicated surface, a more comprehensive model, rather than current geometric models using material removal area, is essentially required to involve the cutting conditions as well as the material properties.

With the F-/STS cutting of micro-structured surfaces, the relationship between the desired surface and corresponding force is very complicated due to the fast oscillations which may inevitably lead to the time-varying cutting directions, cutting speeds, and shear flow directions. In general, these time-varying aspects may further lead to the more complicated material removal behavior. Unfortunately, although F-/STS with force sensing capability was developed, very few results were reported on the investigation of the cutting forces for the generation of freeform and micro-structured surfaces, whether from theoretical or experimental aspect [8, 11]. The unclear features of the cutting forces may significantly block in-depth understandings on the underlying mechanism for material removal in F-/STS as well as the conduction of force controlled generation of complex surfaces.

Although the study of cutting forces was very limited for F-/STS, the prediction of cutting forces in the turning and milling is an old story and has attracted a large amount of attentions. Except from the most common finite element (FE) based numerical models, the mechanistic analytical model is more efficient for fast and explicit estimation of cutting forces [12]. Currently, material removal is believed to be separated by shearing and ploughing mechanisms marked out by the critical chip thickness which is dependent on the edge radius [13–15]. When the DoC beyonds the critical chip thickness, the most direct way for describing the shearing force is to model it as the removal area multiplied by the force coefficient which can be empirically derived from numerous cutting experiments [13–15]. The ploughing mechanism occurs when the DoC is smaller than the critical chip thickness, and this effect is mainly modeled as the cutter indentation into the workpiece. In general, the ploughing force mainly consists of the material recovery and friction components along the radial and tangential directions of the cutter, respectively [14, 16].

Another spectrum of mechanistic force models are developed based on the slip-line field theory.

As a pioneering work, Merchant's force circle developed from a single shear plane significantly influences the following researches in the metal cutting territory [17]. Oxley and his co-authors further developed the slip-line based cutting theory through considering the strain rate and temperature dependent flow stress in terms of the working material and cutting conditions, and the deformation in the secondary deformation zone was also included in the modeling [18, 19]. Based on the Oxley's model, the constitutive relationship for the working material was further extended to the Johnson-Cook model which is the most common one for simulating metal cutting [20, 21]. Moreover, an unequal division shear zone model was developed through considering the non-uniform distribution of the shear velocity, shear strain, and strain rate, and the shear stress and temperature distribution within the primary shear zone could be analytically derived [22]. Through refining the shape of slip-lines in the deformation zone with overall combination of machining conditions and restricted contact cutters, a more universal slip-line model by incorporating the previously developed slip-line field theories was derived by Fang and his co-authors, and [23, 24]. To account for the rounded-edge induced ploughing effect, a simple model was established through analyzing the slip-line field in the third deformation zone [25]. Furthermore, Fang extended his universal slip-line model to describe the machining with a rounded-edge tool [26]. Through dividing the cutting zone into 27 slip-line sub-regions, the shear-zone effect, size-effect, and ploughing effect were described well with usage of a complicatedly shaped cutter [26]. Generally speaking, the generalized models with refined slip-lines are highly qualified for the description of the plastic deformation behavior within the de-formation zones, through providing a microscopic viewpoint for the plastic flow. Despite this, the ultra-fine slip-lines will also make the modeling rather complicated, significantly restricting potential engineering applications for force estimation.

Among these slip-line field based models, the Oxley's model derived on a simple straight shear plane might be the most popular one for the estimation of cutting forces for a variety of cutting processes. Although the Oxley's model is initially proposed for the orthogonal cutting on a basic assumption that the chip flow is approximately steady-state with constant undeformed chip geometry as well as constant cutting conditions [19, 27], it is now widely demonstrated through applying for the milling that the Oxley' model is applicable for the modeling of transient processes with time-varying undeformed chip thickness and cutting velocities [28–31]. Therefore, the single shear band based slip-line field model is employed herein to describe the stress state in the primary deformation zone, and the plastic flow induced cutting force is then obtained through combining the sticking-sliding frictional model at the tool-chip interface. Since the practical DoC remains comparable to the edge-radius in ultra-precision turning [32], the ploughing effect is involved through employing an indentation force model. With respect to the unique cutting kinematics of F-/STS, the time-varying equivalent rake angle, clearance angle, and shear angle are derived and incorporated into both the shearing and ploughing force models. Accordingly, through the edge discretization method [33, 34], the overall cutting force is collected along the radial direction of the cutter with full consideration of the position dependent material removal behavior.

The reminder of this paper is organized as follows: section 2 develops a finite element model to institutionally describe the plastic flow behavior in the deformation zone, and section 3 presents a comprehensive mechanistic model with a beginning of a short description of the cutting kinematics of F-/STS. The estimation results are verified through slow tool servo based experimental turning in section 4, and the main conclusions are drawn in section 5.

2. FE model for F-/STS

The key that F-/STS diamond turning differs from conventional cutting is the oscillated servo motion parallel to the spindle axis, which will simultaneously lead to the time-varying cutting direction and cutting speed, resulting in more complicated plastic flow behavior in the deformation zone. To have a deeper understanding of material removal, a FE model is firstly established with a simple harmonic trajectory imposed on the cutter to mimic F-/STS, and the plastic flow of the material in the deformation zone is accordingly analyzed.

2.1. FE model setup

A two-dimensional FE model is developed using a commercial software ABAQUS. The specially meshed model including a workpiece sizing 80 $\mu m \times 20$ μm and a rounded cutter with edge radius of $r_{\mathrm{e}} = 100$ nm is shown in Fig. 1(a). To simulate the servo motion, the cutter follows a harmonic trajectory with an amplitude of 1 μm (Fig. 1(a)), and the horizontal cutting velocity is set as 2 m/s for the cutter. The nominal DoC is 3 μm, and the nodes at the bottom of the workpiece are fixed. The four-node bilinear plane strain quadrilateral, reduced integration, hourglass control element (CPE4RT) is employed to initially mesh the workpiece and cutter into 62208 and 1264 elements, respectively, and the Lagrangian adaptive meshing strategy is applied to deal with the element distortion during the cutting analysis. Considering the fact that the diamond cutter is much harder than the workpiece material, the cutter is set to be rigid, and the initial temperature for the workpiece and cutter is set as 25 ^{o}C.

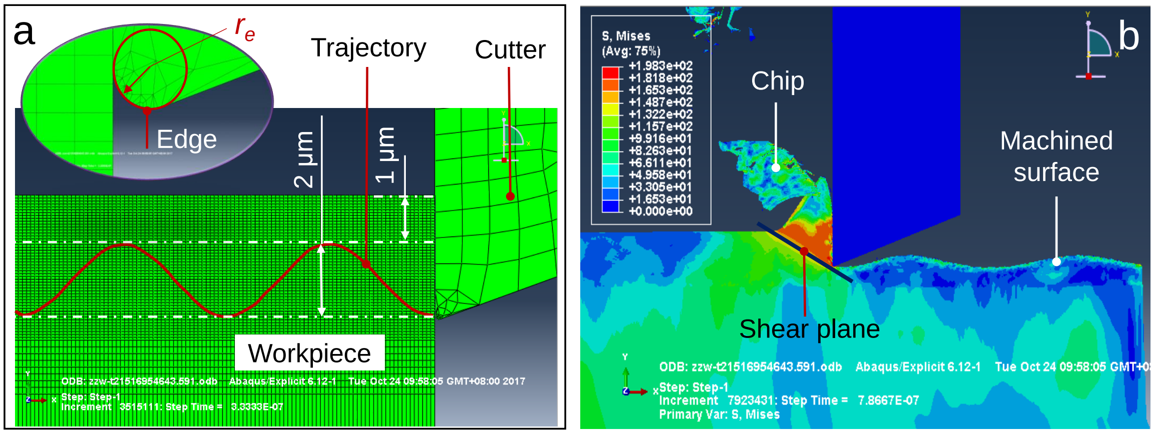

Figure 1: FE model of F-/STS diamond turning, (a) the meshed model at the initial stage, and (b) von Mises stress distribution after cutting.

As for the FE model, the well-known Johnson-Cook model is adopted to describe the constitutive relationship of the working material, and the stress flow inside the shear band with respect to the local strain, strain rate, and temperature can be expressed by [35–37]

$$\sigma_{\mathrm{s}} = (A + B\epsilon_{\mathrm{s}}^{n}) \left[1 + C \ln \left(\frac{\dot{\epsilon_{\mathrm{s}}}}{\dot{\epsilon_0}}\right)\right] \left[1 - \left(\frac{T_{\mathrm{s}} - T_0}{T_{\mathrm{m}} - T_0}\right)^{m}\right] \tag{1}$$

where ϵ and $\dot{\epsilon_{\mathrm{s}}}$ denote the equivalent strain and strain rate, and $\dot{\epsilon}_0$ is a reference strain rate usually taken as 1 s^{-1}. The parameter n and m relates the stress flow with the strain hardening and thermal soften effects of the material, respectively. T_0, T_{s} and T_{m} are the room temperature, working temperature, and melting temperature of the material, respectively. Referring to the parameters summarized in [35, 38], the adopted Johnson-Cook parameters for the used brass are presented in Table 1.

In addition, the Johnson-Cook damage criterion provided by the ABAQUS software is adopted, and the equivalent plastic strain of damage is defined by [39]

$$\epsilon_{\mathrm{f}} = \left[D_1 + D_2 \exp\left(D_3 \frac{\sigma_{\mathrm{m}}}{\bar{\sigma}}\right)\right] \left[1 + D_4 \ln\left(\frac{\dot{\epsilon}^{s}}{\dot{\epsilon_0}}\right)\right] \left[1 + D_5 \left(\frac{T_{\mathrm{s}} - T_0}{T_{\mathrm{m}} - T_0}\right)\right] \tag{2}$$

where σ_{m} and $\bar{\sigma}$ are the average normal stress and von Mises equivalent stress, respectively. The five constants D_i are the damage parameters, which are $D_1 = 0.54$, $D_2 = 4.89$, $D_3 = 3.03$, $D_4 = 0.014$, and $D_5 = 1.12$ as suggested in Ref. [39]. When the increment accumulation of the equivalent plastic strains reaches to the damage strain ϵ_{f}, the fracture of the element is then allowed [39].

To describe the contact behavior between the rake face of the cutter and the chip, a well-known two region model including the sticking and sliding is employed, and the frictional stress can be expressed by [40, 41]

$$\tau_{\mathrm{f}} = \begin{cases} \tau_{\mathrm{st}}, \quad \mu_{\mathrm{e}}\sigma_{\mathrm{n}}(s) \quad \geq \quad \tau_{\mathrm{st}} \\ \mu_{\mathrm{e}}\sigma_{\mathrm{n}}, \ \mu_{\mathrm{e}}\sigma_{\mathrm{n}}(s) < \tau_{\mathrm{st}} \end{cases} \tag{3}$$

where μ_e is the friction coefficient as 0.15 in the FE analysis, and σ_n is the normal stress.

Table 1: Mechanical property of the brass workpiece [35, 38]

A	B	C	m	n	T_m	T_0
9×10^7	2.92×10^8	0.025	1.09	0.31	1083	25

2.2. FE simulation results

The "Dynamic, temp-disp, explicit" method is adopted to solve the model, and the resulting von Mises stress distribution in the cutting zone from step time (st) of 33.33 μs to 54.67 μs is illustrated in Fig. 2 with 9 evenly captured frames. The angle between the horizontal and shear plane (ϕ_o) is a key parameter governing the shearing based material removal behavior. By manually measuring this angle in Fig. 2 through a computer aided design tool, it is observed to decrease from about 37^o to a minimum value of about 27^o at $st = 46.67\mu s$, and then increase to about 32^o. This angle variation mainly attributes to the harmonic trajectory induced time-varying velocity. In general, the velocity variation may lead to a variation of the practical rake angle [42], and the angle variation α_{rv} can be expressed by

$$\alpha_{rv} = \arctan \frac{v_z}{v_0} \tag{4}$$

where v_z and v_0 are the harmonic and horizontal velocity components along the two orthogonal directions, respectively.

To accurately describe the angle ϕ_o, it is separated into one constant angle and one dynamic angle herein. Considering the relationship between the shear angle and the ratio of DoC to chip thickness [20], the angle ϕ_o is improved to be

$$\phi_o = \arctan \frac{\zeta_1 \cos \alpha_{ro}}{1 - \zeta_1 \sin \alpha_{ro}} + \arctan \frac{\zeta_2 \cos \alpha_{rm}}{1 - \zeta_2 \sin \alpha_{rm}} \tag{5}$$

$$\alpha_{rm} = \alpha_{ro} + \alpha_{rv} \tag{6}$$

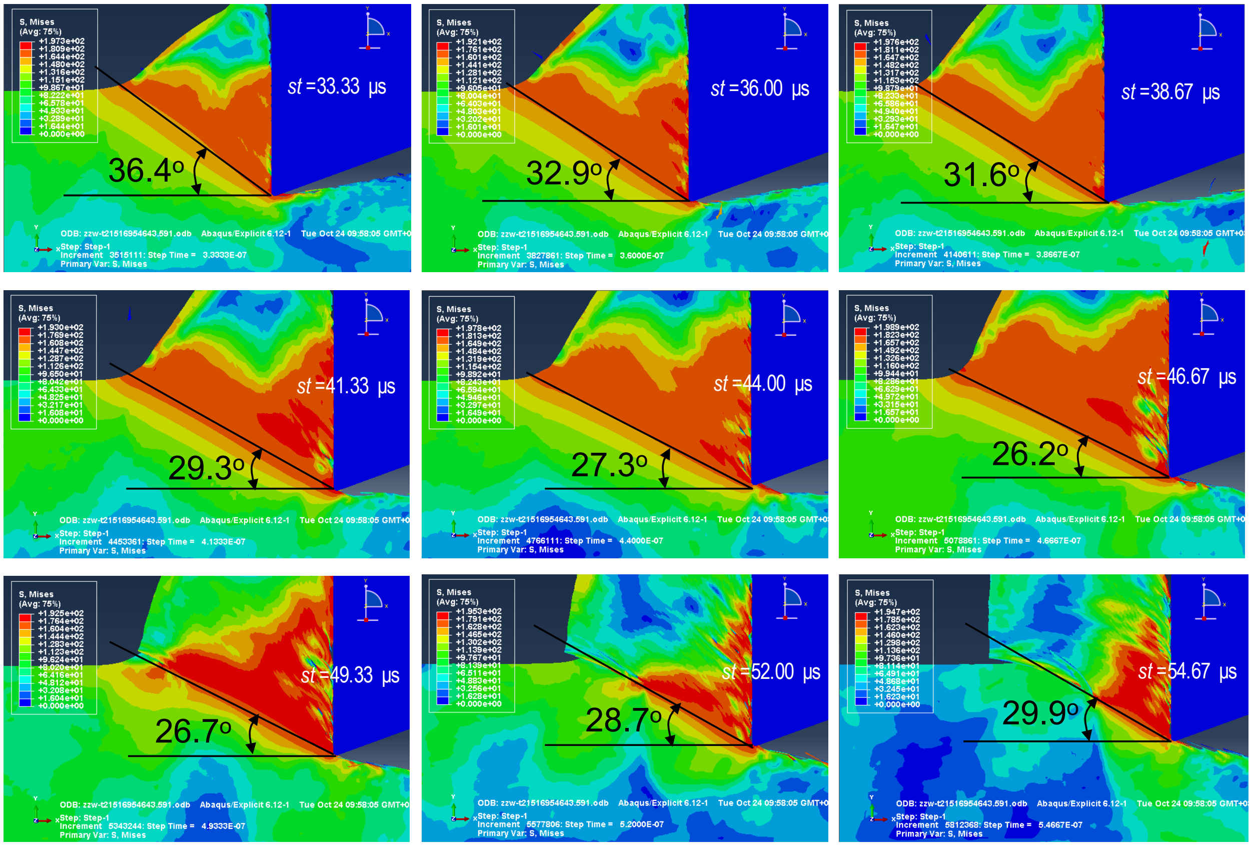

Figure 2: Evolution of stress distribution in the deformation zone with *step-time* (*st*) from 33.33 μs to 54.67 μs.

where α_{ro} is the nominal rake angle, and ζ_1 and ζ_2 are the two equivalent ratios. As defined in Eq. (5), ζ_2 regulates the angle variation, and ζ_1 and ζ_2 jointly determine the angle average.

In general, relationship between the ratio of DoC to the chip thickness and the two equivalent ratios $(\zeta_1,\ \zeta_2)$ should satisfy

$$\arctan\frac{\zeta\cos\alpha_{\mathrm{ro}}}{1-\zeta\sin\alpha_{\mathrm{ro}}}=\arctan\frac{\zeta_1\cos\alpha_{\mathrm{ro}}}{1-\zeta_1\sin\alpha_{\mathrm{ro}}}+\arctan\frac{\zeta_2\cos\alpha_{\mathrm{ro}}}{1-\zeta_2\sin\alpha_{\mathrm{ro}}}\tag{7}$$

If the cutter has a zero rake angle which is very commonly adopted in diamond turning, the requirement in Eq. (7) can be simplified to be

$$\zeta=\frac{\zeta_1+\zeta_2}{1-\zeta_1\zeta_2}\tag{8}$$

By setting $\zeta_1 = \zeta_2 = 0.35$ and $\alpha_{\mathrm{ro}} = 0$, the estimated angle ϕ_{o} from Eq. (5) is illustrated in Fig. 3 which correspond to the 9 frames illustrated in Fig. 2. In addition, the 9 angles measured from the FE results are also presented in Fig. 3. A good agreement between the FE and analytical results is observed, suggesting that the proposed model in Eq. (5) can characterize well the tendency of the angle ϕ_{o} with respect to the velocity variation.

Remark 1: With the conventional shear angle model (left term in Eq. (7)), the shear angle only depends on the ratio ζ for a given cutter. However, this ratio may also vary in F-/STS due to the time-varying cutting conditions. In addition, certain other time-varying factors including the cutting direction, cutting velocity, and friction angle may jointly contribute to the variation of the angle ϕ_{o}. Therefore, two equivalent ratios ζ_1 and ζ_2 are necessary to simultaneously capture the average and variation of this key angle.

Remark 2: The FE simulation result demonstrates the time-varying characteristics of the material removal behavior, which is induced by the inherent oscillations in F-/STS. Moreover, the derived relationship between the shear angle and oscillation parameters can provide a reliable basis for the development of the mechanistic cutting force model.

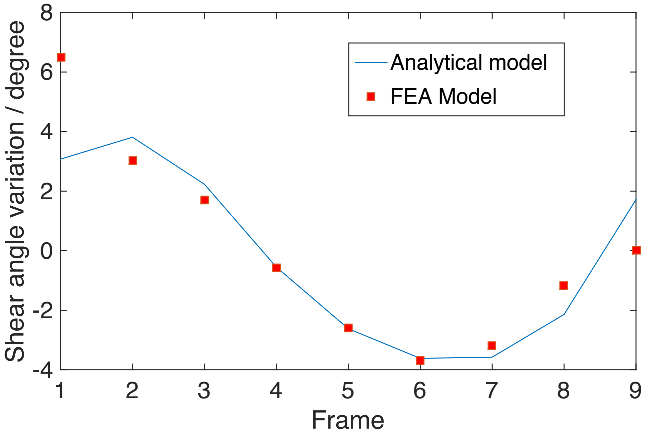

Figure 3: Angle variation of the shear plane relative to the horizontal plane.

3. Mechanistic cutting force model for F-/STS

To model the position dependent cutting forces, kinematics of F-/STS is firstly introduced for the generation of micro-structured surfaces. During turning, the removal zone is defined as the engagement of the cutter areas in any two successive cutting points along the radial direction of the workpiece, and it is evenly discretized into finite pieces. Material removal for each cutting piece is equivalently modeled as an orthogonal cutting process. Accordingly, the overall cutting force for a given position is obtained through summarizing the forces generated by all the pieces at this position.

3.1. Kinematics of F-/STS

As illustrated in Fig. 4(a), $o_\mathrm{m}-x_\mathrm{m}y_\mathrm{m}z_\mathrm{m}$ is the Cartesian coordinate system fixed on the machine tool. The $o_\mathrm{m}-x_\mathrm{m}z_\mathrm{m}$ plane is parallel to the planar motion of the slides, and $o_\mathrm{m}z_\mathrm{m}$ coincides with the spindle axis. The projected views of the cutter and desired surface in the $o_\mathrm{m}-y_\mathrm{m}z_\mathrm{m}$ and $o_\mathrm{m}-x_\mathrm{m}z_\mathrm{m}$ planes are further shown in Figs. 4(b) and (c), respectively. Essentially, the turning operation is conducted in a cylindrical coordinate system $(\rho, \varpi, z_\mathrm{m})$. By setting $x_\mathrm{m} = \rho\cos\varpi$ and $y_\mathrm{m} = \rho\sin\varpi$, the desired micro-structured surface can be mathematically described in this cylindrical system as $z_\mathrm{s} = S(\rho\cos\varpi, \rho\sin\varpi)$ with $S(\cdot)$ denoting the mathematical function for the surface.

The trajectory for F-/STS is evenly discretized into N cutter location points (CLPs) for one revolution of the spindle. Since the edge radius is much smaller than the servo motion, the rounded-edge effect is ignored for the trajectory calculation. During cutting, the cutter tip is aligned with the rotational center, and the CLP is set as the nose center of the cutter. Assume the diamond cutter approaches from the outer space to the center of the workpiece, the radial and angular positions for the l-th CLP in the k-th revolution ($o_{k,l}$) can be respectively expressed by

$$\rho_{k,l} = \rho_\mathrm{max} - \left(k + \frac{l}{N} - 1\right) f_\mathrm{s} \tag{9}$$

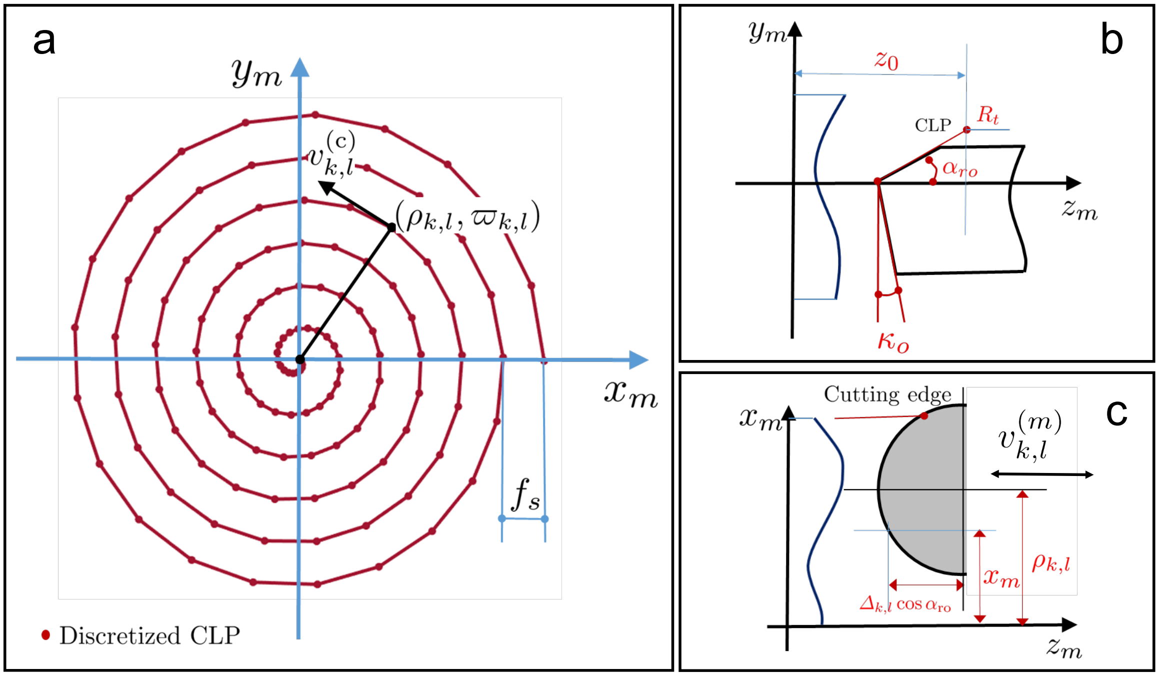

Figure 4: Schematic of cutting kinematics of STS diamond turning, (a) the spiral toolpath with discretized CLP, (b) the lateral and (c) top view of the cutting process.

$$\varpi_{k,l} = 2(k-1)\pi + \frac{2\pi l}{N} \tag{10}$$

where $\rho_{\max}$ is the radius of the workpiece, N is the angular sampling ratio for one revolution, and f_{s} denotes the feedrate per revolution along the x_{m}-axial direction.

At the CLP $o_{k,l}$, the velocity component induced by the spindle rotation can be expressed by

$$v_{k,l}^{(\mathrm{c})} = \frac{\pi n}{30} \rho_{k,l} \tag{11}$$

where n is the number of revolutions per minute of the spindle.

From that projected on the $o_{\mathrm{m}} - x_{\mathrm{m}} z_{\mathrm{m}}$ plane in Fig. 4(c), the z_{m}-axial coordinate of the cutter edge described in the $o_{\mathrm{m}} - x_{\mathrm{m}} y_{\mathrm{m}} z_{\mathrm{m}}$ system can be expressed by

$$z_{k,l}^{(\mathrm{t})} = z_0 + (R_{\mathrm{t}} - \mathit{\Delta}_{k,l}) \cos \alpha_{\mathrm{ro}} \tag{12}$$

$$\mathit{\Delta}_{k,l} = \sqrt{R_{\mathrm{t}}^2 - \left[x_{\mathrm{m}} - \rho_{k,l}\right]^2} \tag{13}$$

where $x_{\mathrm{m}} \in [\rho_{k,l} - R_{\mathrm{t}}, \rho_{k,l} + R_{\mathrm{t}}]$, and R_{t} is the nose radius of the employed diamond cutter. z_0 represents the pre-set z_{m}-axial virtual position of the cutter tip, which is adopted to guarantee that the cutter is above the desired surface during toolpath calculation [43].

Through projecting the cutter edge along the z_{m}-axial direction, the corresponding profile of the edge on the desired surface can be expressed in the $o_{\mathrm{m}} - x_{\mathrm{m}}y_{\mathrm{m}}z_{\mathrm{m}}$ system by

$$z_{k,l}^{(\mathrm{s})} = S\left(\rho_{k,l}\cos\varpi_{k,l}, \rho_{k,l}\sin\varpi_{k,l} + (R_{\mathrm{t}} - \mathit{\Delta}_{k,l})\sin\alpha_{\mathrm{ro}}\right) \tag{14}$$

To avoid over-cut, the required servo motion for F-/STS along the z_{m}-axial direction is the minimum distance between the cutter edge and the corresponding projected profile on the surface [43], which can be expressed by

$$z_{k,l}^{(\mathrm{m})} = \min\left\{z_{k,l}^{(\mathrm{t})} - z_{k,l}^{(\mathrm{s})}\right\} - z_0,\ \forall x_{\mathrm{m}} \in [\rho_{k,l} - R_{\mathrm{t}}, \rho_{k,l} + R_{\mathrm{t}}] \tag{15}$$

Therefore, with the CLP $o_{k,l}$, the servo velocity along the z_{m}-axial direction can be obtained as

$$v_{k,l}^{(\mathrm{m})} = \frac{z_{k,l}^{(\mathrm{m})} - z_{k,l-1}^{(\mathrm{m})}}{60} nN \tag{16}$$

3.2. Shearing force model for orthogonal cutting

To derive the shearing force, the Oxley's model is firstly employed to obtain the shearing stress for chip flow with respect to the thermoplastic properties of the workpiece material, tool geometry, and cutting conditions. Before implementing the Oxley's model, several basic assumptions are made as follows:

a). The cutter is perfectly sharp. Although the rounded-edge is non-ignorable as aforementioned, the sharp tool assumption is satisfied here through defining an equivalent rake face which linearly connects the lowest cutting point at the edge and the highest equivalent contact point [16].

b). Considering the fact that the practical DoC is commonly much smaller than the cutter radius in F-/STS, the material removal can be modeled as the plane strain deformation through the plane strain plasticity theory [19, 27].

c). The shearing is represented by one straight slip-line near the center of the parallel-sided primary deformation zone with directions being approximately coincident with the maximum shear strain rate and maximum shear stress [19, 28, 29]. Considering the transient nature of F-/STS, this assumption is over simplified to some extent. However, the result from milling processes with time-varying features suggests that this is acceptable for high accurate prediction of cutting forces [28–31].

d). The shear strain, shear strain rate, and temperature are uniform along the shear plane. Although non-uniform distribution described by different governing laws is proposed to extend the Oxley's model [22, 30], the uniform distribution using average values is adopted in this study as that used in many cases to simplify the modeling [28, 29, 31].

e). The forces in F-/STS corresponding to the condition changes have the values for the same conditions in the steady-state. This assumption is supported by experiment results from the milling process [28].

3.2.1. Stress model in the deformation zone

As aforementioned, the cutting region is discretized into finite pieces. Without loss of generality, a schematic of the material removal for the *i*-th cutting piece is illustrated in Fig. 5. As for each cutting piece, when the practical DoC is larger than the critical chip thickness, the material is removed through shearing based plastic flow.

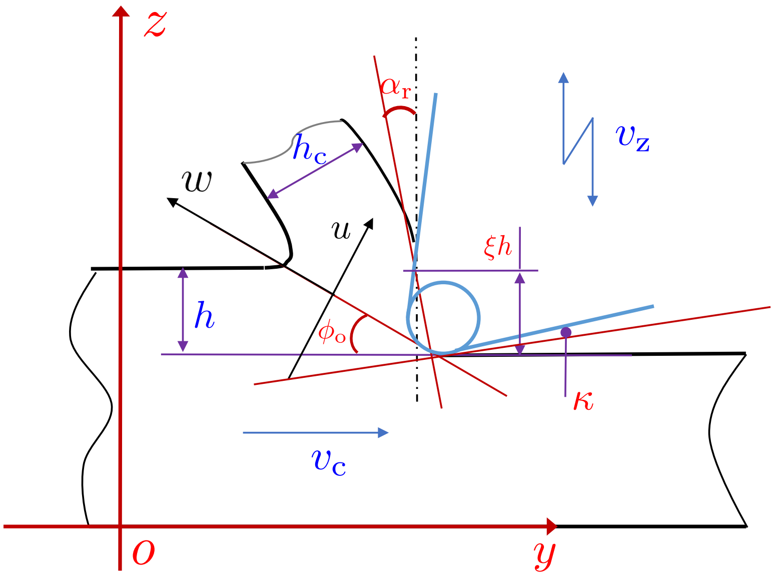

Figure 5: Schematic of material removal in orthogonal cutting, where h is short for $h_{k,l}^{(i)}$.

Considering the cutter with rounded-edge, when the practical DoC goes down to be comparable to the value of the edge radius, the effective rake angle of the cutter will tend to be negative [16, 44]. Recall the definition in Eq. (4), by setting $v_0 = v_{k,l}^{(\mathrm{c})}$ and $v_\mathrm{z} = v_{k,l}^{(\mathrm{m})}$, the equivalent rake angle α_r related to the practical DoC, tool edge radius, and cutting velocity for the i-th cutting piece can be expressed by

$$\begin{aligned} \alpha_\mathrm{r} &= \alpha_\mathrm{rv} + \alpha_\mathrm{re} \\ &= \arctan \frac{v_{k,l}^{(\mathrm{m})}}{v_{k,l}^{(\mathrm{c})}} - \arctan \frac{\delta}{\xi h_{k,l}^{(i)}} \end{aligned} \tag{17}$$

where $\xi \geq 1$ is a multiple factor determining the equivalent contact height. As suggested in [44], the upper boundary of this factor should satisfy $\xi h_{k,l}^{(i)} < l_\mathrm{st}$ with l_st and $h_{k,l}^{(i)}$ denoting the sticking length of the chip on the rake face and the practical DoC for the i-th cutting piece at CLP $o_{k,l}$, respectively. In addition, δ denotes the distance from the lowest cutting point at the edge to a vertical line passing through the highest equivalent contact point.

Recall the definition of the velocity induced rake angle in Eq. (6), the distance δ can be expressed by [16, 44]

$$\delta = \begin{cases} -r_{\mathrm{e}} \cos \varphi, & \xi h_{k,l}^{(i)} \leq r_{\mathrm{e}} \left(1 + \sin \alpha_{\mathrm{rm}}\right) \\ \dfrac{\xi h_{k,l}^{(i)} - r_{\mathrm{e}} \left(1 + \sin \alpha_{\mathrm{rm}}\right)}{\cot \alpha_{\mathrm{rm}}} - r_{\mathrm{e}} \cos \alpha_{\mathrm{rm}}, & \xi h_{k,l}^{(i)} > r_{\mathrm{e}} \left(1 + \sin \alpha_{\mathrm{rm}}\right) \end{cases} \tag{18}$$

with

$$\varphi = \arcsin \frac{\xi h_{k,l}^{(i)} - r_{\mathrm{e}}}{r_{\mathrm{e}}} \tag{19}$$

In metal cutting, the shear angle is defined as the relative angle between the shear plane and the cutting direction. It may vary with respect to the motion along the z_{m}-axial direction as well as the profile of previously generated surface [45, 46]. Considering the two effects and the angle ϕ_{o} defined in Eq. (5), the practical instantaneous shear angle ϕ can be expressed by

$$\phi = \phi_{\mathrm{o}} + \phi_{\mathrm{s}} + \phi_{\mathrm{m}} \tag{20}$$

with

$$\phi_{\mathrm{s}} = \arctan \frac{\dot{z}_{\mathrm{s}}(i)}{v_{k,l}^{(\mathrm{c})}}, \ \phi_{\mathrm{m}} = \alpha_{\mathrm{rv}} = \arctan \frac{v_{k,l}^{(\mathrm{m})}}{v_{k,l}^{(\mathrm{c})}} \tag{21}$$

where $\dot{z}_{\mathrm{s}}(i)$ denotes the local slope of the desired surface corresponding to the position of the i-th cutting piece at the CLP $o_{k,l}$.

Assume the relative cutting velocity is $v_{k,l}$ which is a combination of the two components $v_{k,l}^{(\mathrm{m})}$ and $v_{k,l}^{(\mathrm{c})}$ along the z_{m} and y_{m}-axial directions. Following the triangular principle, the velocity along the shear band for the i-th cutting piece can be obtained as

$$v_{\mathrm{s}} = \frac{\cos\left(\phi_{\mathrm{m}} + \alpha_{\mathrm{r}}\right)}{\cos\left(\phi_{\mathrm{o}} - \alpha_{\mathrm{r}}\right)} v_{k,l} \tag{22}$$

$$v_{k,l} = \sqrt{\left(v_{k,l}^{(\mathrm{m})}\right)^2 + \left(v_{k,l}^{(\mathrm{c})}\right)^2} \tag{23}$$

Accordingly, the shear strain in the shear band can be estimated to be

$$\gamma_{\mathrm{s}} = \frac{1}{2}\frac{v_{\mathrm{s}}}{v_{\perp}} = \frac{\cos\left(\phi_{\mathrm{m}} + \alpha_{\mathrm{r}}\right)}{2\sin\phi\cos\left(\phi_{\mathrm{o}} - \alpha_{\mathrm{r}}\right)} \tag{24}$$

where $v_{\perp}$ is the velocity component vertical to the shear plane.

Through adopting the Oxley factor C_{ox} relating to cutting conditions and material properties [18, 19], the corresponding stain rate in the shear band can be expressed by

$$\dot{\gamma_{\mathrm{s}}} = \frac{C_{\mathrm{ox}} v_{\mathrm{s}}}{l_{\mathrm{s}}} = \frac{C_{\mathrm{ox}}\cos\left(\phi_{\mathrm{m}} + \alpha_{\mathrm{r}}\right)\sin\phi_{\mathrm{o}}}{2h_{k,l}^{(i)}\cos\left(\phi_{\mathrm{o}} - \alpha_{\mathrm{r}}\right)} v_{k,l} \tag{25}$$

where l_{s} denotes the length of the shear band, and the Oxley factor C_{ox} is simplified to be constant which was demonstrated to be applicable even for conditions with time-varying undeformed chip thickness and cutting velocity [29].

Similar to that used in FE model, the Johnson-Cook model in Eq. (1) is employed to describe the material constitutive relationship. Using the von Mises criterion, the shear stress, shear strain, and shear strain rate can be related to the equivalent stress, strain, and strain rate through

$$\tau_{\mathrm{s}} = \frac{\sigma_{s}}{\sqrt{3}}, \ \gamma_{\mathrm{s}} = \sqrt{3}\epsilon_{\mathrm{s}}, \ \dot{\gamma_{\mathrm{s}}} = \sqrt{3}\dot{\epsilon_{\mathrm{s}}} \tag{26}$$

Therefore, the Johnson-Cook model governing the plastic flow inside the shear band can be rewritten as

$$\sqrt{3}\tau_{\mathrm{s}} = \mathit{\Gamma}_{\mathrm{JC}}\left[1 - \left(1 - \frac{T_{\mathrm{m}} - T_{\mathrm{s}}}{T_{\mathrm{m}} - T_{0}}\right)^{m}\right] \tag{27}$$

$$\mathit{\Gamma}_{\mathrm{JC}} = \left[A + B\left(\frac{\gamma_{\mathrm{s}}}{\sqrt{3}}\right)^{n}\right]\left[1 + C\ln\left(\frac{\dot{\gamma_{\mathrm{s}}}}{\sqrt{3}}\right)\right] \tag{28}$$

Generally speaking, there are three physical processes that may determine the temperature balance inside the shear band, namely heat generated by plastic working, heat diffusion, and material convection [47, 48]. To simplify the modeling, the energy balance inside the shear band is approximated to be

$$\rho\chi\left(T_{\mathrm{s}}-T_0\right)=(1-\eta)\,\tau_{\mathrm{s}}\gamma_{\mathrm{s}} \tag{29}$$

where ρ and χ are the density and specific heat of the workpiece material, and the factor η accounts for the heat loss.

With the assumption that the working temperature is close to the melting temperature of the material, the Taylor formula is employed to linearize Eq. (27) by neglecting the high-order small quantity of the temperature term. Therefore, the equilibrium shear stress inside the shear band can be explicitly obtained through combining Eq. (27), (28), and (29) as

$$\tau_{\mathrm{s}}=\frac{m\rho\chi\left(T_{\mathrm{m}}-T_0\right)}{\sqrt{3}\rho\chi\left(T_{\mathrm{m}}-T_0\right)+m\left(1-\eta\right)\gamma_{\mathrm{s}}\mathit{\Gamma}_{\mathrm{JC}}}\mathit{\Gamma}_{\mathrm{JC}} \tag{30}$$

As shown in Fig. 5, assume that $o-uw$ is the local coordinate system fixed at the shear band with the u- and w axes being vertical and parallel to the shear plane, respectively. Based on the equilibrium equations of the ideal slip-line field, the stress equilibrium inside the shear band can be expressed in this $o-uw$ system by [19, 20]

$$\frac{\partial\sigma}{\partial u}=\frac{\partial\tau}{\partial w}=\frac{\partial\tau}{\partial\gamma}\frac{\partial\gamma}{\partial t}\frac{\partial t}{\partial w}+\frac{\partial\tau}{\partial\dot{\gamma}}\frac{\partial\dot{\gamma}}{\partial w}+\frac{\partial\tau}{\partial T_s}\frac{\partial T_s}{\partial w} \tag{31}$$

Considering the assumption that the strain rate reaches maximum at the shear plane ($\dfrac{\partial\dot{\gamma}}{\partial w}=0$) and the temperature gradient is ignorantly small $\dfrac{\partial T_s}{\partial w}=0$), an integration of both sides of Eq. 31 (can be simplified to be:

$$\int\frac{\partial\sigma}{\partial u}\mathrm{d}u=\int\frac{\partial\tau}{\partial w}\mathrm{d}u \tag{32}$$

Therefore, it leads to the relationship between stresses at the two ends of the shear band as shown in Fig. 6 to be

$$\sigma_{\mathrm{s}1} - \sigma_{\mathrm{s}2} = \frac{h_{k,l}^{(i)}\dot{\gamma}_{\mathrm{s}}}{\sin\phi_{\mathrm{o}} v_{\perp}} \frac{\partial \tau}{\partial \gamma} \tag{33}$$

By combining Eq. (27) and Eq. (28), the term $\partial\tau/\partial\gamma$ can be derived as [20]:

$$\frac{\partial \tau}{\partial \gamma} = \frac{nB\gamma_{\mathrm{s}}^{n-1}}{A\left(\sqrt{3}\right)^{n} + B\gamma_{\mathrm{s}}}\tau_{\mathrm{s}} \tag{34}$$

Through substituting Eq. (24), Eq. (25), and Eq. (34) into Eq. (33), the stress at the bottom end of the shear band can be obtained as

$$\sigma_{\mathrm{s}2} = \sigma_{\mathrm{s}1} - 2\tau_{\mathrm{s}} n \frac{BC_{\mathrm{ox}}\gamma_{\mathrm{s}}^{n}}{\sqrt{3}^{n} A + B\gamma_{\mathrm{s}}} \tag{35}$$

Taking account of the cutter oscillations in F-/STS, the free surface will be no longer parallel to the cutting velocity. This inclination will disturb the stress boundary condition described by the Hencky's equation to derive the stress $\sigma_{\mathrm{s}1}$ [19, 30]. In F-/STS, the oscillation velocity is relatively small with respect to the main cutting velocity at any CLPs, which is strictly restricted by the allowable clearance angle of the cutter to avoid undesired interference between the cutter and workpiece [2, 49]. Considering this fact, the effects on the boundary conditions will be negligibly small as suggested by Oxley and his co-authors [28]. Therefore, the equivalent stress $\sigma_{\mathrm{s}1}$ inside the shear band at the free surface can be expressed by [19, 30]

$$\sigma_{\mathrm{s}1} = \tau_{\mathrm{s}}\left[1 + 2\left(\frac{\pi}{4} - \phi\right)\right] \tag{36}$$

3.2.2. Shearing force model

With the Oxley's model, a free chip model is developed to obtain the complete slip-line field model based on an equilibrium between the shear stress at the tool-chip interface as well as the shear flow stress in the secondary deformation zone. This complete model requires an assumption of normally distributed stress at the tool-chip interface with a constant thickness of the secondary deformation zone. This assumption remains to have a conflict with the experimental observations [20, 50]. Moreover, the modeling accuracy for the complete model highly depends on the temper-ature variation as well as the thermoplastic behavior of the chip which is usually difficult to be determined accurately with respect to different kinds of materials. Therefore, without relying on these assumptions, a simpler and more practical stress model at the tool-chip interface is adopted through assuming a constant frictional coefficient.

Following this strategy, the equivalent interface contact length between the rake face of the cutter and the generated chip is firstly defined through a slip-line field based geometry model by [51]

$$l_{\mathrm{ct}} = \frac{2h_{k,l}^{(i)} \cos\left(\alpha_{\mathrm{re}} - \phi_{\mathrm{o}}\right)}{\sin \phi_{\mathrm{o}}} \tag{37}$$

Accordingly, with this contact region shown in Fig. 6, the normal stress distribution at a point having a distance to the lowest point at the cutter edge to be s can be expressed by [20]

$$\sigma_{\mathrm{n}}(s) = \sigma_{\mathrm{no}} \left[1 - \left(\frac{s}{l_{\mathrm{ct}}}\right)^{a}\right] \tag{38}$$

where a is a constant characterizing the stress distribution. Considering the stress boundary condition at the bottom of the shear plane, the normal stress on the rake face should be equal to the hydrostatic stress in the shear plane, namely $\sigma_{\mathrm{no}} = \sigma_{\mathrm{s2}}$ [11, 19, 28].

Therefore, the normal force on the cutter can be obtained through integrating the stress along

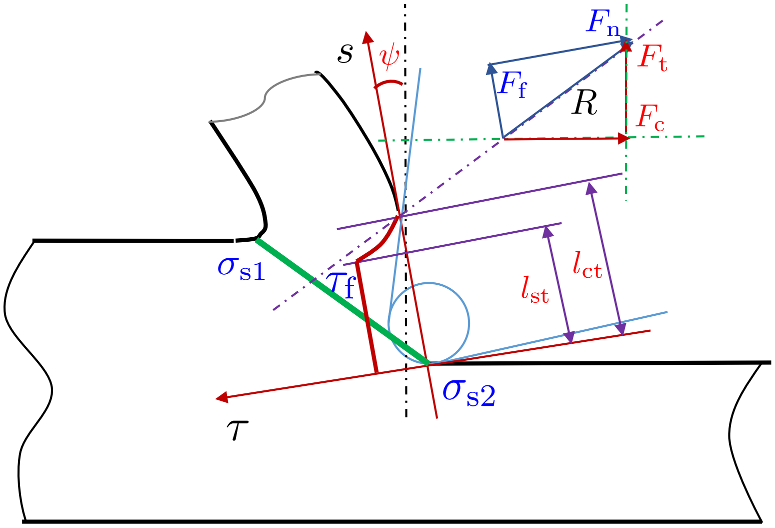

Figure 6: Schematic of stress distribution in the tool-chip interface.

the whole contact length, which yields

$$F_\mathrm{n}(i) = \int_0^{l_\mathrm{ct}} \Lambda_{k,l}^{(i)} \sigma_\mathrm{n}(s)\mathrm{d}s = k_\mathrm{n}\sigma_\mathrm{s2}\frac{\cos\left(\alpha_\mathrm{re}-\phi_\mathrm{o}\right)\Lambda_{k,l}^{(i)} h_{k,l}^{(i)}}{\sin\phi_\mathrm{o}} \tag{39}$$

$$k_\mathrm{n} = \frac{2a}{a+1} \tag{40}$$

where $\Lambda_{k,l}^{(i)}$ is the width of the i-th cutting piece at the CLP $o_{k,l}$.

As for the frictional stress, recall the definition in Eq. 3, the stress distribution is modeled to be as that shown in Fig. 6, with one sticking region and one sliding region at the cutter-chip interface. With the region near the cutting edge, the sticking friction occurs with the shearing stress being constantly distributed. Meanwhile, with the reminder part, the sliding friction occurs with shearing stress being proportional to the corresponding normal stress. Mathematically, the overall shearing stress imposed on the cutter can be expressed by [20, 40, 41]

$$\tau_\mathrm{f} = \begin{cases} \tau_\mathrm{st}, & s \in [o, l_\mathrm{st}] \\ \mu_\mathrm{e}\sigma_\mathrm{n}(s), & s \in (l_\mathrm{st}, l_\mathrm{ct}]) \end{cases} \tag{41}$$

where μ_{e} is the friction coefficient, and the sticking length l_{st} is assumed to be half of the contact length to simplify the modeling.

With the assumption that the frictional shear stress at the transfer point from the sticking to the sliding region is continuous, the frictional shear stress in the sticking region can be expressed by

$$\tau_{\mathrm{st}} = \mu_{\mathrm{e}}\sigma_{\mathrm{n}}(l_{\mathrm{st}}) = \mu_{\mathrm{e}}\sigma_{\mathrm{s2}}\left(1 - 2^{-a}\right) \tag{42}$$

By integrating the frictional shear stress along the whole contact region, the frictional force can be expressed by

$$F_{\mathrm{f}}(i) = \int_0^{l_{\mathrm{st}}} w\tau_{\mathrm{st}}\mathrm{d}s + \int_{l_{\mathrm{st}}}^{l_{\mathrm{ct}}} \mu_{\mathrm{e}} w\sigma_{\mathrm{n}}(s)\mathrm{d}s = k_{\mathrm{f}}\mu_{\mathrm{e}}\sigma_{\mathrm{s2}}\frac{\cos\left(\alpha_{\mathrm{re}} - \phi_{\mathrm{o}}\right) w_{k,l}^{(i)} h_{k,l}^{(i)}}{\sin\phi_{\mathrm{o}}} \tag{43}$$

with the equivalent proportionality factor k_{f} being expressed by

$$k_{\mathrm{f}} = 1 - 2^{-a} + \frac{2^{a+1} - 1}{2^{a}\left(a + 1\right)} \tag{44}$$

As shown in Fig. 6, the equivalent contact angle ψ is defined as the included angle between the vertical line and the line from the lowest point at the edge to the cutter-chip separation point at the rake face. It can be obtained from the geometry relationship as

$$= \begin{cases} \arccos\left(\dfrac{l_{\mathrm{ct}}}{2r_{\mathrm{e}}}\right), & l_{\mathrm{ct}} \leq l_{\mathrm{e}} \\ \arcsin\left[\dfrac{r_{\mathrm{e}}\left(1 + \tan\alpha_{\mathrm{ro}}\right)\cos\alpha_{\mathrm{ro}}}{l_{\mathrm{ct}}}\right] - \alpha_{\mathrm{ro}}, & l_{\mathrm{ct}} > l_{\mathrm{e}} \end{cases} \tag{45}$$

$$l_{\mathrm{e}} = \frac{\sqrt{2}r_{\mathrm{e}}\cos\alpha_{\mathrm{ro}}}{\sqrt{1 - \sin\alpha_{\mathrm{ro}}}} \tag{46}$$

Accordingly, the main cutting force $F_{\mathrm{c}}(i)$ and the thrust force $F_{\mathrm{t}}(i)$ for the i-th cutting piece during shearing based material removal can be determined by

$$\begin{cases} F_{\mathrm{c}}(i) = F_{\mathrm{n}}(i)\cos\psi + F_{\mathrm{f}}(i)\sin\psi \\ F_{\mathrm{t}}(i) = F_{\mathrm{f}}(i)\cos\psi - F_{\mathrm{n}}(i)\sin\psi \end{cases} \tag{47}$$

3.3. Ploughing force modeling

When the nominal DoC is smaller than the critical chip thickness h_{s}, the material can not be removed through plastic flow. Instead, ploughing with partial elastic deformation of the material will occur beneath the rounded cutter. The ploughing force can be commonly modeled to be proportional to the interference volume [16, 52, 53]. To simplify the modeling process, the critical chip thickness is modeled as a proportion of the edge radius, which is [36, 54]:

$$h_{\mathrm{s}} = r_{\mathrm{e}}\left(1 - \cos\varrho\right) \tag{48}$$

where ϱ is the angular position of the point at the cutting edge with critical chip thickness, and it is approximate to be constant with $\cos\varrho = 0.75$.

Similar to the variation of the practical shear angle, the practical clearance angle can be obtained through considering both the z_{m}-axial motion and the local surface profile, which can be expressed by

$$\kappa = \kappa_{\mathrm{o}} + \arctan\frac{v_{k,l}^{(\mathrm{m})}}{v_{k,l}^{(\mathrm{c})}} - \arctan\frac{\dot{z}_{\mathrm{s}}(i)}{v_{k,l}^{(\mathrm{c})}} \tag{49}$$

where κ_{o} is the nominal clearance angle of the cutter.

Since the edge radius is in the nanometer scale, the local surface profile interfered with the cutter can be approximate to be a straight line. For a given DoC, the interference area can be expressed by [16]

$$S_{\mathrm{p}}(i)=\begin{cases} r_{\mathrm{e}}^{2}\left(\vartheta-0.5\sin 2\vartheta\right), & h_{k,l}^{(i)}\in[0,h_{\mathrm{r}}] \\ \dfrac{1}{2}\left[r_{\mathrm{e}}^{2}\left(\vartheta+\kappa\right)-r_{\mathrm{e}}\left(r_{\mathrm{e}}-h_{k,l}^{(i)}\right)\left(\sin\vartheta+\sin\kappa\right)+\left(h_{k,l}^{(i)}-h_{\mathrm{r}}\right)^{2}\tan^{-1}\kappa\right], & h_{k,l}^{(i)}\in(h_{\mathrm{r}},h_{\mathrm{s}}] \end{cases} \tag{50}$$

where

$$h_{\mathrm{r}}=r_{\mathrm{e}}\left(1-\cos\kappa\right),\ \vartheta=\arccos\left(1-\frac{h_{k,l}^{(i)}}{r_{\mathrm{e}}}\right) \tag{51}$$

Therefore, the ploughing force and the corresponding frictional force can be determined by

$$\begin{cases} F_{\mathrm{c,p}}(i)=\mu_{\mathrm{p}}k_{\mathrm{int}}\mathit{\Lambda}_{k,l}^{(i)}S_{\mathrm{p}}(i) \\ F_{\mathrm{t,p}}(i)=k_{\mathrm{int}}\mathit{\Lambda}_{k,l}^{(i)}S_{\mathrm{p}}(i) \end{cases} \tag{52}$$

where μ_{p} is the friction coefficient for the ploughing.

Assume the cutting force is continuous with respect to the DoC, the proportion ratio k_{int} can be determined through combining Eq. (39), Eq. (43), and Eq. (52) by

$$k_{\mathrm{int}}=\sqrt{\frac{k_{\mathrm{n}}^{2}+\left(\mu_{\mathrm{e}}k_{\mathrm{f}}\right)^{2}}{1+\mu_{\mathrm{p}}^{2}}}\frac{\sigma_{\mathrm{s2}}\cos\left(\alpha_{\mathrm{re}}-\phi_{\mathrm{o}}\right)h_{\mathrm{s}}}{\sin\phi_{\mathrm{o}}S_{\mathrm{p}}|_{h_{k,l}^{(i)}=h_{\mathrm{s}}}} \tag{53}$$

3.4. Cutting force in F-/STS

A schematic of the tool engagement is illustrated in Fig. 7 with the cutter being at the l-th CLP in the $(k-1)$-th and the k-th revolution. The free surface of the workpiece is assumed to be planar, and $o_{\mathrm{t}}-x_{\mathrm{t}}z_{\mathrm{t}}$ is defined as the local coordinate system on the rake face of the cutter with the $o_{\mathrm{t}}z_{\mathrm{t}}$ axis passing through the CLP $o_{k,l}$ and the $o_{\mathrm{t}}x_{\mathrm{t}}$ axis being parallel to the free surface. Following the edge discretization principle, the engaged region $\widehat{ABC}$ is evenly discretized by dividing the included angle $\angle A o_{k,l} C$ into N_{t} pieces. Considering the cutting kinematics, the relative distance between the two CLPs $o_{k-1,l}$ and $o_{k,l}$ can be expressed by

$$d_{k,l} = \sqrt{f_s^2 + \left(z_{k-1,l}^{(\mathrm{m})} - z_{k,l}^{(\mathrm{m})}\right)^2} \tag{54}$$

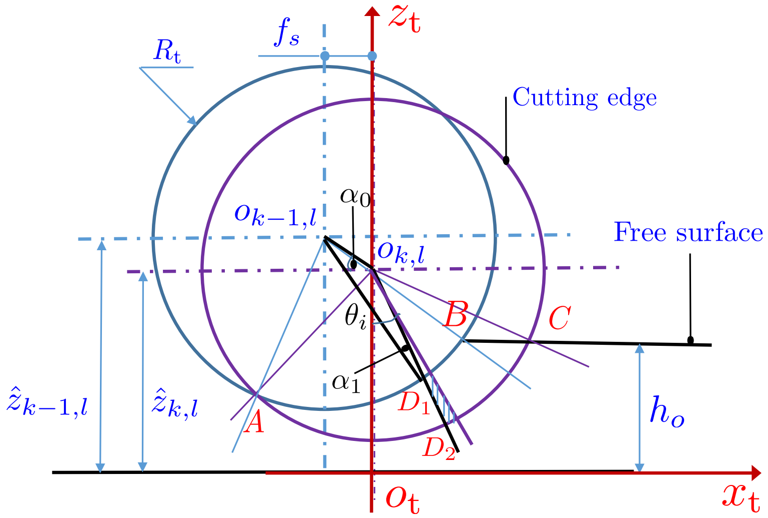

Figure 7: Schematic of the instantaneous material removal in F-/STS.

With respect to the i-th cutting piece D_1D_2 shown in Fig 7, the included angle α_0 between the vector $\overrightarrow{o_{k-1,l}o_{k,l}}$ and the $o_{\mathrm{t}}x_{\mathrm{t}}$ axis can be expressed by

$$\alpha_0 = \arctan\left(\frac{z_{k-1,l}^{(\mathrm{m})} - z_{k,l}^{(\mathrm{m})}}{f_{\mathrm{s}}}\right) \tag{55}$$

Therefore, the directional vector of $\overrightarrow{o_{k-1,l}o_{k,l}}$ can be obtained as $\mathbf{u} = [-\cos\alpha_0, \sin\alpha_0]$. Since $\triangle A o_{k-1,l} o_{k,l}$ is an isosceles triangle, the position of point A, i.e. $P_a = [x_{\mathrm{a}}, z_{\mathrm{a}}]$, can be determined in the $o_{\mathrm{t}} - x_{\mathrm{t}} z_{\mathrm{t}}$ system by:

$$\begin{bmatrix} x_{\mathrm{a}} \\ z_{\mathrm{a}} \end{bmatrix} = \frac{1}{2}\begin{bmatrix} -f_{\mathrm{s}} \\ z_{k-1,l}^{(\mathrm{m})} + z_{k,l}^{(\mathrm{m})} \end{bmatrix} + \sqrt{R_{\mathrm{t}}^2 - \left(\frac{d_{k,l}}{2}\right)^2}\begin{bmatrix} -\sin\alpha_0 \\ -\cos\alpha_0 \end{bmatrix} \tag{56}$$

In addition, since the two points B and C are at the free surface, the z_{t}-axial coordinates of the two points are equal, i.e., $z_\mathrm{b} = z_\mathrm{c} = h_\mathrm{o}$. According to the geometry relationship, the x_t-axial coordinates of the two points can be respectively expressed by

$$\begin{cases} x_\mathrm{b} = \sqrt{R_\mathrm{t}^2 - \left(z_{k-1,l}^{(\mathrm{m})} - h_\mathrm{o}\right)^2} - f_\mathrm{s} \\ x_\mathrm{c} = \sqrt{R_\mathrm{t}^2 - \left(z_{k,l}^{(\mathrm{m})} - h_\mathrm{o}\right)^2} \end{cases} \tag{57}$$

Accordingly, the relative angle of $\overrightarrow{o_{k,l}A}$, $\overrightarrow{o_{k,l}B}$, and $\overrightarrow{o_{k,l}C}$ with respect to the $o_\mathrm{t}z_\mathrm{t}$ axis can be obtained as

$$\begin{cases} \theta_\mathrm{a} = \arcsin\left(\dfrac{x_\mathrm{a}}{R_\mathrm{t}}\right) \\ \theta_\mathrm{b} = \arctan\left(\dfrac{x_\mathrm{b}}{z_{k,l}^{(\mathrm{m})} - h_o}\right) \\ \theta_\mathrm{c} = \arcsin\left(\dfrac{x_\mathrm{c}}{R_\mathrm{t}}\right) \end{cases} \tag{58}$$

Following the triangulation principle, the included angle α_1 between $\overrightarrow{o_{k-1,l}D_1}$ and $\overrightarrow{o_{k,l}D_1}$ can be determined by

$$\alpha_1 = \arcsin\left[\frac{d_{k,l}}{R_\mathrm{t}}\cos\left(\alpha_0 + \theta_i\right)\right] \tag{59}$$

where θ_i is the relative angle between the i-th cutting piece and the $o_\mathrm{t}z_\mathrm{t}$ axis.

Therefore, considering the nominal rake angle (α_ro) of the cutter, the practical DoC for the i-th cutting piece can be mathematically modeled through a piece-wise function as

$$h_{k,l}^{(i)} = \begin{cases} \left[1 - \dfrac{\cos\left(\alpha_0 + \theta_i + \alpha_1\right)}{\cos\left(\alpha_0 + \theta_i\right)}\right] R_\mathrm{t}\cos\alpha_\mathrm{ro}, & \theta_i \in [\theta_\mathrm{a}, \theta_\mathrm{b}] \\ R_\mathrm{t}\cos\alpha_\mathrm{ro} - \dfrac{z_{k,l}^{(\mathrm{m})} - h_o}{\cos\theta_i}\cos\alpha_\mathrm{ro}, & \theta_i \in (\theta_\mathrm{b}, \theta_\mathrm{c}] \end{cases} \tag{60}$$

The corresponding width for the i-th cutting piece at the CLP $o_{k,l}$ can be expressed by

$$\Lambda_{k,l}^{(i)} = \frac{\theta_\mathrm{c} - \theta_\mathrm{a}}{N_\mathrm{t}} R_\mathrm{t} \tag{61}$$

With the developed shearing and ploughing force models, the overall main cutting force and thrust force at the CLP $o_{k,l}$ can be obtained as

$$F_{k,l}^{(\mathrm{c})} = \sum \left\{ F_{\mathrm{c,p}}\left(i\right) \middle| \forall h_{k,l}^{(i)} < h_{\mathrm{s}} \right\} + \sum \left\{ F_{\mathrm{c}}\left(i\right) \middle| \forall h_{k,l}^{(i)} > h_{\mathrm{s}} \right\} \tag{62}$$

$$F_{k,l}^{(\mathrm{t})} = \sum \left\{ F_{\mathrm{t,p}}\left(i\right) \middle| \forall h_{k,l}^{(i)} < h_{\mathrm{s}} \right\} + \sum \left\{ F_{\mathrm{t}}\left(i\right) \middle| \forall h_{k,l}^{(i)} > h_{\mathrm{s}} \right\} \tag{63}$$

4. Experimental results and discussion

4.1. Experimental setup

Experimental turning through slow tool servo diamond turning was conducted on an ultra-precision lathe (350 FG, Moore Nanotechnology, USA), and a micro-structured harmonic grid surface was generated for the demonstration. A natural single crystal diamond cutter is adopted for material removal. The nose radius of the cutter is 0.103 mm, and the nominal rake angle and clearance angle are 0 and 7 degree, respectively. A brass cylinder with radius of $\rho_{\max} = 3\ mm$ is employed as the workpiece for the turning. To capture the cutting force, a three-axial dynamometer (9255b, Kistler Group, Germany) was assembled beneath the diamond cutter as photographically shown in Fig. 8, and the sampling ratio for the force measurement is set as 50 kHz.

During cutting, the spindle speed is set to be 15 rpm, and the feedrate along the x_{m}-axial direction is 5 $\mu m/rev$. The nominal DoC is set as 8 μm. To guarantee acceptable interpolation error along the cutting direction, the sampling ratio for toolpath calculation is set as $N = 1200$ per revolution. After cutting, the three dimensional (3-D) micro-topography of the generated surface was captured and characterized by a non-contact optical surface profiler (Nexview, Zygo Corporation, USA).

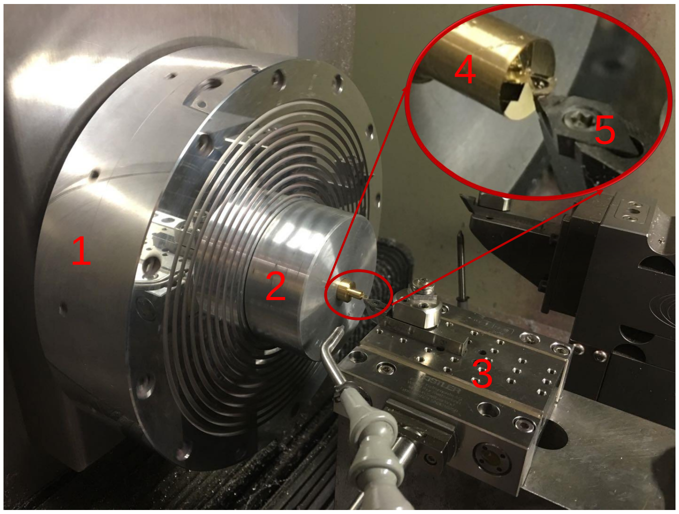

Figure 8: Photograph of the cutting system with: 1. spindle, 2. fixture for the workpiece, 3. three-axial dynamometer, 4. brass workpiece, and 5. diamond cutter.

Without loss of generality, the desired micro-structured surface is mathematically described by

$$S(x_{\mathrm{m}}, y_{\mathrm{m}}) = A_{\mathrm{x}} \sin(2\pi f_{\mathrm{sx}} x_{\mathrm{m}}) + A_{\mathrm{y}} \sin(2\pi f_{\mathrm{sy}} y_{\mathrm{m}}) \tag{64}$$

where $A_{\mathrm{x}} = A_{\mathrm{y}} = 1.25\ \mu m$ is the amplitude of the periodic micro-structured surface, and $f_{\mathrm{sx}} = f_{\mathrm{sy}} = 2.5\ /mm$ is the spatial frequency along the two directions. The 3-D features of the practically generated surface were captured through a 20× projection lens and illustrated in Fig. 9.

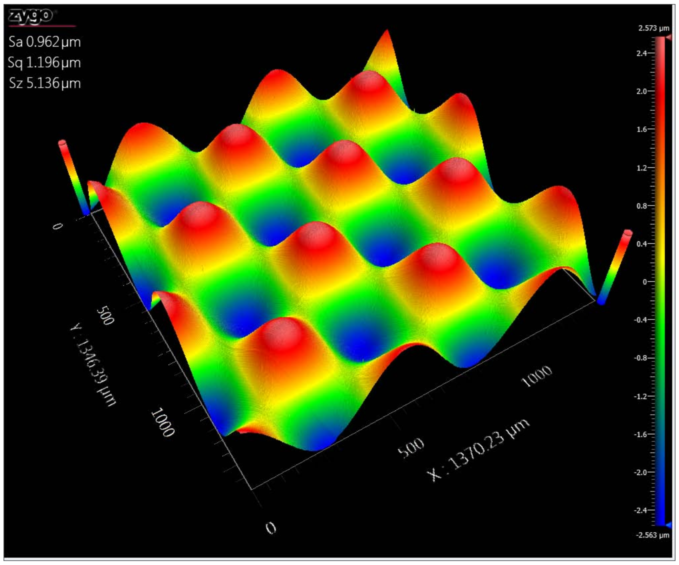

Figure 9: 3-D micro-topography of the generated micro-structured surface.

4.2. *Cutting force verification*

To verify the developed cutting force model, the main and thrust cutting forces during one revolution of the spindle was extracted at the position of $\rho = 1.415\ mm$. The adopted z_{m}-axial servo motion during this revolution is shown in Fig. 10(a), and the servo velocity induced angle variation α_{rv} as defined in Eq. (4) is illustrated in Fig. 10(b). With the edge discretization, the engaged region is only sliced into $N_{\mathrm{t}} = 30$ pieces to reduce the computational burden, and the average DoC at each CLP is calculated and illustrated in Fig. 10(c) in terms of the rotational angle of the spindle. It is observed that the average DoC varies from about 0.5 μm to 1 μm, and it is much smaller than the nominal DoC (8 μm). Considering the edge radius, this result suggests that the rounded-edge effect is non-ignorable during diamond turning even using large nominal DoC.

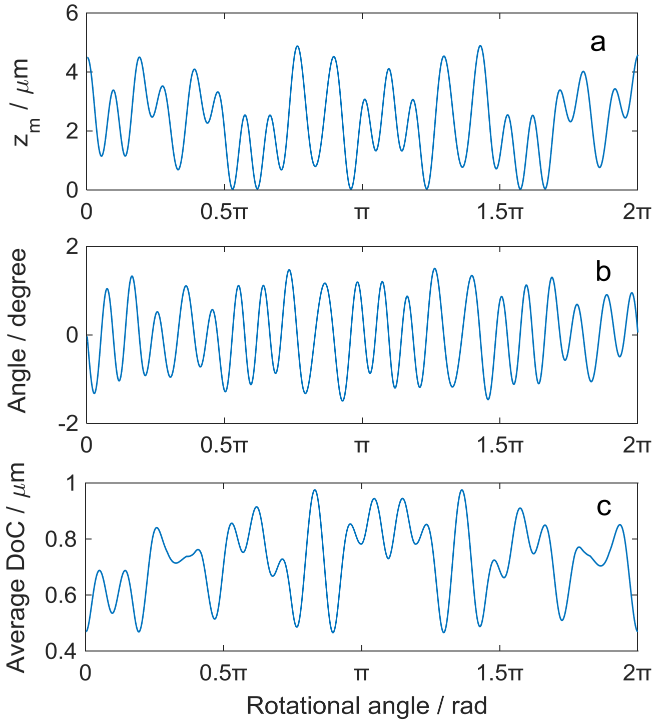

Figure 10: Related kinematic components during one revolution at $\rho = 1.415\ mm$, (a) the z_{m}-axial servo motion, (b) the angle variation induced by the servo motion, and (c) the average DoC.

To show more details about features of material removal, the practical DoCs at the 25-th, 125-th, and 500-th CLPs during this revolution is illustrated in Fig. 11(a) with respect to the cutting pieces.

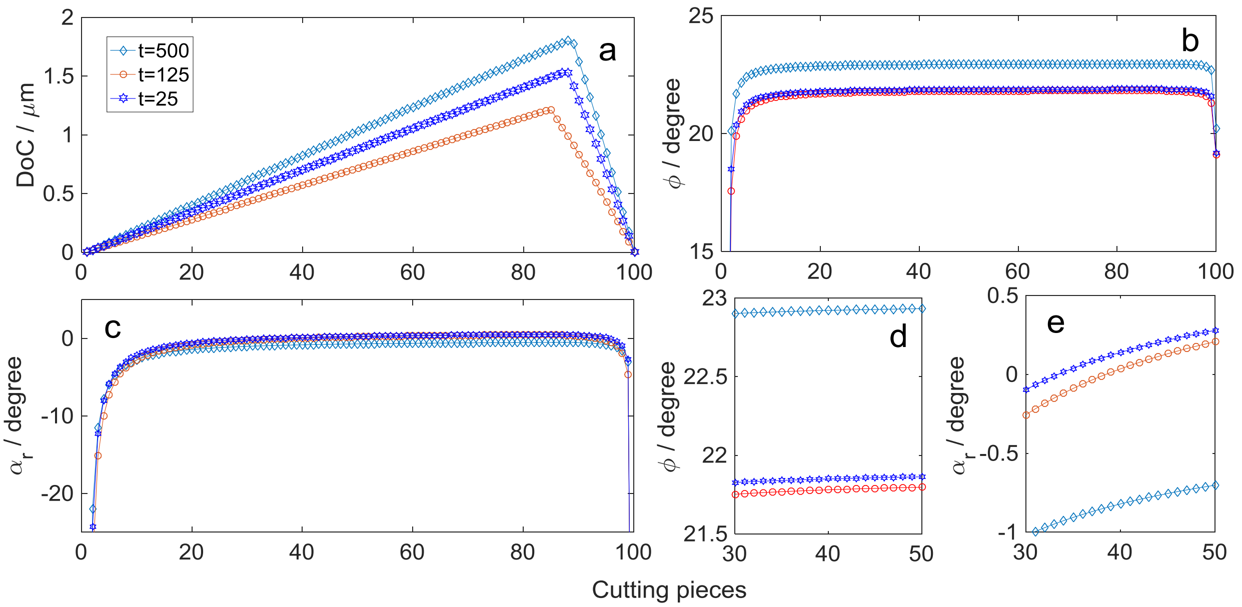

Figure 11: Intermediate variables at different CLPs with respect to the discretized cutting pieces, (a) the practical DoC, (b) the practical shear angle, (c) the practical rake angle, (d) enlarged view of the practical shear angle, and (e) enlarged view of the practical rake angle.

Herein, the cutting edge is discretized into $N_{\mathrm{t}} = 100$ pieces to better show the features. In addition, the estimated practical shear angle ϕ and rake angle α_{r} in shearing are illustrated in Figs. 11(b) and 11(c) with correspondingly enlarged views being shown in Figs. 11(d) and 11(e), respectively. As shown in Fig. 11, when the practical DoC gets smaller, the practical rake angle becomes more negative, and accordingly resulting in much smaller shear angle. Moreover, the practical rake angles and shear angles are observed to differ to the ones at different CLPs, which might jointly attribute to the position dependent cutting velocity and position dependent DoC. This result suggests that the developed mechanistic model can capture position-dependent features of process parameters related to material removal in F-/STS diamond turning.

Table 2: Adopted parameters for the analytical model

α_{ro}	0	κ_{o}	7^{o}
ζ_1	0.0875	μ_{e}	0.075
ζ_2	0.32	μ_{p}	0.15
χ	450 J/kg$\cdot^{o}$C	ξ	2
η	0.37	a	0.85
C_{ox}	8	r_{e}	50 nm

To estimate the analytically simulated cutting forces, parameters for the Johnson-Cook constitutive model are set as the same of that shown in Table 1, and the parameters for the analytical model are identified as shown in Table 2. The geometric parameters of the cutter are set as the practical one used in the turning, and the edge radius is directly set as $r_e = 50$ nm which is an average value as widely accepted for the diamond cutters. Considering the heat diffusion (30%) and material convection (10%), the ratio for total heat loss is estimated to be $\eta = 1 - (1 - 0.3) \times (1 - 0.1) = 0.37$. In addition, the constant parameters μ_{p}, ζ_2, and ξ are reasonably set as shown in Table 2. The four more important parameters, a, ζ_1, μ_{e}, and C_{ox}, are identified through trail and error method manually. Although the cutter is just sliced into 30 pieces, the computation of the estimated forces is still time consuming. Therefore, only the practical and estimated forces from 0 to $t = 0.2$ s are used for identifying the four parameters. The estimated forces from $t = 0.2$ s to $t = 3$ s are then calculated by the identified model and compared with the practical forces to verify the developed model.

Corresponding to the cutting kinematics shown in Fig. 10, the estimated main cutting force and thrust force are illustrated in Fig. 12(a) and Fig. 14, respectively. Since the practically captured force is relatively small and is strongly coupled with noises, a low pass filter with cut-off frequency of 100 Hz is employed to pre-process the measured cutting forces. The practical main cutting force after filtering is comparatively illustrated in Fig. 12(a), and an enlarged view in Fig. 12(b) gives a more detailed comparison of the estimated and practical main cutting forces from $t = 1.5$ s to $t = 3$ s, showing a good accordance with each other. To give a quantitative evaluation of the modeling accuracy, the resulting modeling error is further given in Fig. 13, showing a maximum error of about ±0.005 N.

The estimated and filtered practical thrust force are also presented in Fig. 14. The thrust force is in general much smaller than the main cutting force, and the amplitude is in the same level of the coupled system noises. As shown in Fig. 14, although it is filtered, the practical thrust force is observed to be coupled with strong noises. However, the main tendency of the practical thrust force remains very consistent with the estimated one, demonstrating the effectiveness of the developed mechanistic force model for the characterization of the time-varying cutting forces in F-/STS.

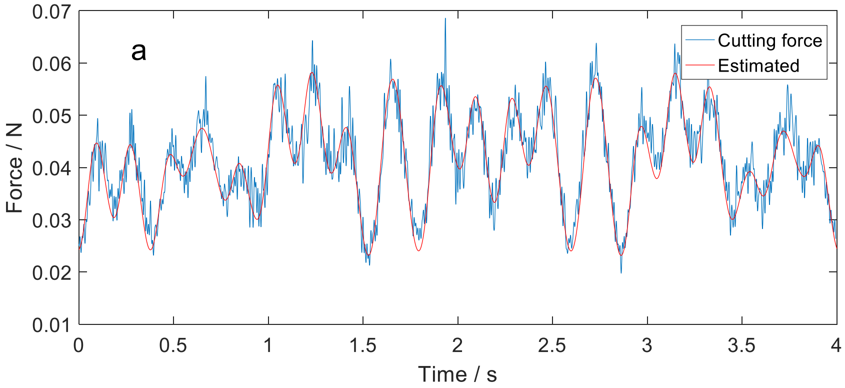

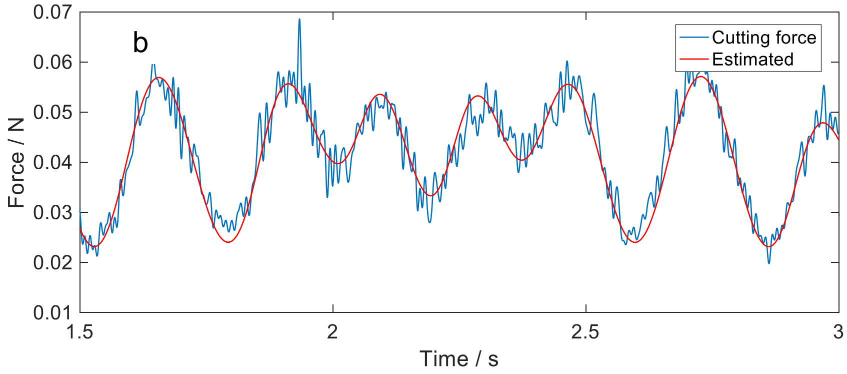

Figure 12: Characteristics of the practical and estimated main cutting force, (a) the cutting force in one revolution of the spindle, and (b) an enlarged view of the forces from 1.5 s to 3 s.

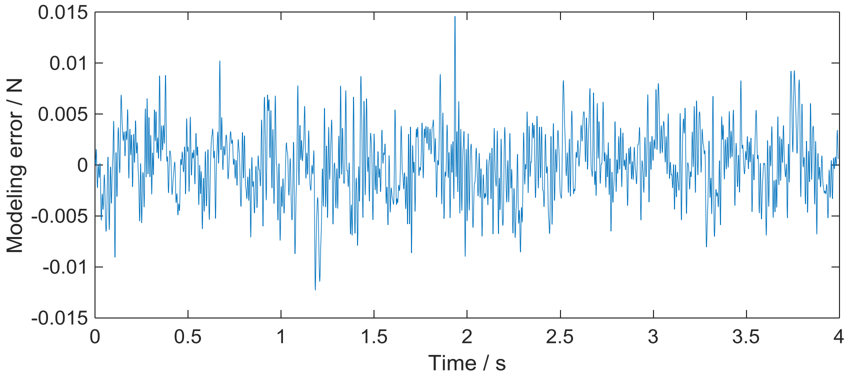

Figure 13: Modeling error of the main cutting force.

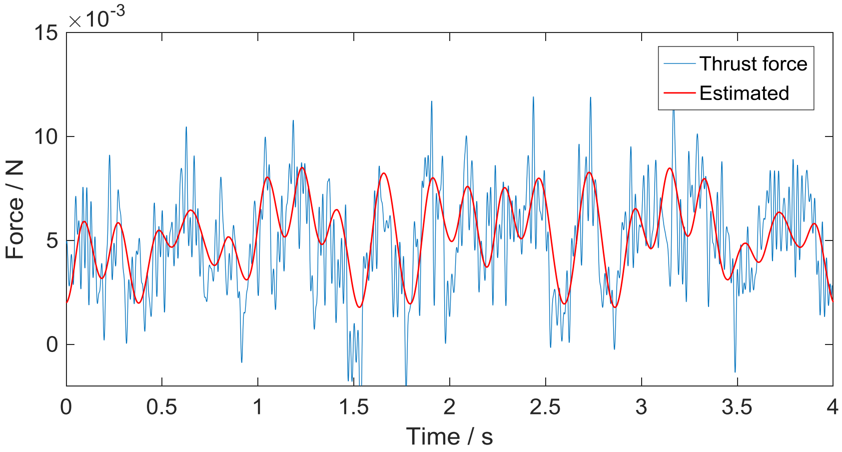

Figure 14: Characteristics of the practical and estimated thrust force.

5. Conclusions

Considering the servo motion induced dynamic features of material removal, a comprehensive mechanistic force model was developed for fast-/slow tool servo (F-/STS) diamond turning of micro-structured surfaces. To facilitate the understanding of plastic flow in shearing, a finite element (FE) model is firstly introduced to simulate the F-/STS turning. The FE result shows that the relative angle between the shear plane and horizontal plane varies significantly with respect to the simulation time, attributing to the oscillated servo motion. Considering this effect, a prediction model is developed in terms of equivalent chip ratios and servo velocity dependent practical rake angles, and a good agreement is achieved for the FE and analytical results.

Considering the cutting kinematics, the edge discretization method suggests that the practical depth-of-cut (DoC) is much smaller than the nominal DoC for any cutter location points, and a certain amount of the discretized cutting pieces have practical DoCs comparable to the edge radius of the cutter, suggesting that the rounded-edge effect is non-ignorable in diamond turning. To describe this effect, a cutter with sharp edge is adopted by using an equivalent rake angle which is geometrically determined by the chip-cutter contact length and the lowest point at the cutting edge. In addition, shearing and ploughing mechanisms are considered through comparing the practical

DoC with the critical chip thickness for each cutting piece.

The slip-line field theory is employed to describe the shearing based material removal. The oscillated servo motion introduces the velocity dependent rake angles and clearance angles. Moreover, shear angle, shear strain, shear strain rate, temperature, and stress distribution inside the shear band also vary with respect to the oscillated servo motion. These variable factors together with the variable DoC jointly contribute to the time-varying shearing cutting force and frictional force. With respect to the cutting pieces having DoC smaller than the critical chip thickness, the corresponding ploughing force is modeled to be proportionate to the interference volume between the cutter and workpiece.

At each cutter location point, the main cutting force and thrust force can be obtained through summarizing the forces acting on all the discretized cutting pieces. Experimental turning is conducted to generate a typical micro-structured surface through slow tool servo diamond turning. The practical main cutting force and thrust force exhibit a good agreement with the theoretically estimated ones, demonstrating the effectiveness of the developed mechanistic model for describing cutting forces in F-/STS.

Acknowledgments

This work was jointly supported by the National Natural Science Foundation of China (51705254, 51675455), the Natural Science Foundation of Jiangsu Province (BK20170836), and the Fundamental Research Funds for the Central Universities (30917011301, 309171A8804).

References

[1] X.-D. Lu, D. Trumper, Ultrafast tool servos for diamond turning, CIRP Annals 54 (1) (2005) 383 – 388.

[2] D. P. Yu, S. W. Gan, Y. S. Wong, G. S. Hong, M. Rahman, J. Yao, Optimized tool path generation for fast tool servo diamond turning of micro-structured surfaces, The International Journal of Advanced Manufacturing Technology 63 (9) (2012) 1137–1152.

[3] Z. Zhu, S. To, Adaptive tool servo diamond turning for enhancing machining efficiency and surface quality of freeform optics, Opt. Express 23 (16) (2015) 20234–20248.

[4] D. P. Yu, G. S. Hong, Y. S. Wong, Profile error compensation in fast tool servo diamond turning of micro-structured surfaces, International Journal of Machine Tools and Manufacture 52 (1) (2012) 13 – 23.

[5] M. Mukaida, J. Yan, Ductile machining of single-crystal silicon for microlens arrays by ultra-precision diamond turning using a slow tool servo, International Journal of Machine Tools and Manufacture 115 (2017) 2 – 14.

[6] S. To, Z. Zhu, H. Wang, Virtual spindle based tool servo diamond turning of discontinuously structured microoptics arrays, CIRP Annals 65 (1) (2016) 475 – 478.

[7] E. Brinksmeier, O. Riemer, R. Glbe, B. Lnemann, C. Kopylow, C. Dankwart, A. Meier, Sub-micron functional surfaces generated by diamond machining, CIRP Annals 59 (1) (2010) 535 – 538.

[8] Y.-L. Chen, Y. Cai, K. Tohyama, Y. Shimizu, S. Ito, W. Gao, Auto-tracking single point diamond cutting on non-planar brittle material substrates by a high-rigidity force controlled fast tool servo, Precision Engineering 49 (2017) 253 – 261.

[9] G. Herrera-Granados, N. Morita, H. Hidai, S. Matsusaka, A. Chiba, K. Ashida, I. Ogura, Y. Okazaki, Development of a non-rigid micro-scale cutting mechanism applying a normal cutting force control system, Precision Engineering 43 (2016) 544 – 553.

[10] X. Zhou, R. Wang, Q. Liu, Study on suppressing cutting force fluctuations based on chip loads for turning optical freeform surfaces, The International Journal of Advanced Manufacturing Technology 90 (5) (2017) 2037–2046.

[11] Y. Altintas, M. Eynian, H. Onozuka, Identification of dynamic cutting force coefficients and chatter stability with process damping, CIRP Annals 57 (1) (2008) 371 – 374.

[12] P. Arrazola, T. zel, D. Umbrello, M. Davies, I. Jawahir, Recent advances in modelling of metal machining processes, CIRP Annals 62 (2) (2013) 695 – 718.

[13] X. Zhang, K. F. Ehmann, T. Yu, W. Wang, Cutting forces in micro-end-milling processes, International Journal of Machine Tools and Manufacture 107 (2016) 21 – 40.

[14] Z. Kilic, Y. Altintas, Generalized mechanics and dynamics of metal cutting operations for unified simulations, International Journal of Machine Tools and Manufacture 104 (2016) 1 – 13.

[15] P. Huang, W. Lee, Cutting force prediction for ultra-precision diamond turning by considering the effect of tool edge radius, International Journal of Machine Tools and Manufacture 109 (2016) 1 – 7.

[16] M. P. Vogler, S. G. Kapoor, R. E. DeVor, On the modeling and analysis of machining performance in micro-endmilling, part ii: Cutting force prediction, Journal of Manufacturing Science and Engineering 126 (4) (2004) 695–705.

[17] M. E. Merchant, Mechanics of the metal cutting process. i. orthogonal cutting and a type 2 chip, Journal of Applied Physics 16 (5) (1945) 267–275.

[18] P. Oxley, Development and application of a predictive machining theory, Machining Science and Technology 2 (2) (1998) 165–189.

[19] P. Oxley, W. Hastings, Predicting the strain rate in the zone of intense shear in which the chip is formed in machining from the dynamic flow stress properties of the work material and the cutting conditions, in: Proceedings of the Royal Society of London A: Mathematical, Physical and Engineering Sciences, Vol. 356, The Royal Society, 1977, pp. 395–410.

[20] T. Özel, E. Zeren, A methodology to determine work material flow stress and tool-chip interfacial friction properties by using analysis of machining, Journal of manufacturing science and Engineering 128 (1) (2006) 119–129.

[21] X. Jin, Y. Altintas, Slip-line field model of micro-cutting process with round tool edge effect, Journal of Materials Processing Technology 211 (3) (2011) 339 – 355.

[22] B. Li, Y. Hu, X. Wang, C. Li, X. Li, An analytical model of oblique cutting with application to end milling, Machining Science and Technology 15 (4) (2011) 453–484.

[23] N. Fang, I. S. Jawahir, Analytical predictions and experimental validation of cutting force ratio, chip thickness, and chip back-flow angle in restricted contact machining using the universal slip-line model, International Journal of Machine Tools and Manufacture 42 (6) (2002) 681–694.

[24] N. Fang, I. S. Jawahir, P. L. B. Oxley, A universal slip-line model with non-unique solutions for machining with curled chip formation and a restricted contact tool, International Journal of Mechanical Sciences 43 (2) (2001) 557–580.

[25] D. J. Waldorf, R. E. Devor, S. G. Kapoor, A slip-line field for ploughing during orthogonal cutting, Journal of Manufacturing Science and Engineering 120 (4) (1998) 693–699.

[26] N. Fang, Slip-line modeling of machining with a rounded-edge toolpart i: new model and theory, Journal of the Mechanics and Physics of Solids 51 (4) (2003) 715 – 742.

[27] R. Roth, P. L. B. Oxley, Slip-line field analysis for orthogonal machining based upon experimental flow fields, Journal of Mechanical Engineering Science 14 (2) (1972) 85–97.

[28] H.-T. Young, P. Mathew, P. Oxley, Predicting cutting forces in face milling, International Journal of Machine Tools and Manufacture 34 (6) (1994) 771–783.

[29] Z. Wang, M. Rahman, Y. Wong, X. Li, A hybrid cutting force model for high-speed milling of titanium alloys, CIRP Annals-Manufacturing Technology 54 (1) (2005) 71–74.

[30] L. Pang, A. Hosseini, H. Hussein, I. Deiab, H. Kishawy, Application of a new thick zone model to the cutting mechanics during end-milling, International Journal of Mechanical Sciences 96 (2015) 91–100.

[31] H. Zheng, X. Li, Y. Wong, A. Nee, Theoretical modelling and simulation of cutting forces in face milling with cutter runout, International Journal of Machine Tools and Manufacture 39 (12) (1999) 2003–2018.

[32] Y.-L. Chen, Y. Cai, M. Xu, Y. Shimizu, S. Ito, W. Gao, An edge reversal method for precision measurement of cutting edge radius of single point diamond tools, Precision Engineering 50 (2017) 380 – 387.

[33] S. Campocasso, J. P. Costes, G. Fromentin, S. Bissey-Breton, G. Poulachon, A generalised geometrical model of turning operations for cutting force modelling using edge discretisation, Applied Mathematical Modelling 39 (21) (2015) 6612–6630.

[34] A. Lamikiz, L. L. de Lacalle, J. Snchez, M. Salgado, Cutting force estimation in sculptured surface milling, International Journal of Machine Tools and Manufacture 44 (14) (2004) 1511 – 1526.

[35] G. R. Johnson, W. H. Cook, A constitutive model and data for metals subjected to large strains, high strain rates and high temperatures, in: Proceedings of the 7th International Symposium on Ballistics, Vol. 21, The Netherlands, 1983, pp. 541–547.

[36] X. Lai, H. Li, C. Li, Z. Lin, J. Ni, Modelling and analysis of micro scale milling considering size effect, micro cutter edge radius and minimum chip thickness, International Journal of Machine Tools and Manufacture 48 (1) (2008) 1 – 14.

[37] L. Zhou, F. Peng, R. Yan, P. Yao, C. Yang, B. Li, Analytical modeling and experimental validation of micro end-milling cutting forces considering edge radius and material strengthening effects, International Journal of Machine Tools and Manufacture 97 (2015) 29–41.

[38] N. Fang, Sensitivity analysis of the material flow stress in machining, in: ASME 2003 International Mechanical Engineering Congress and Exposition, American Society of Mechanical Engineers, 2003, pp. 23–32.

[39] G. R. Johnson, W. H. Cook, Fracture characteristics of three metals subjected to various strains, strain rates, temperatures and pressures, Engineering fracture mechanics 21 (1) (1985) 31–48.

[40] R. Xiong, H. Wu, Study on cutting mechanism of ti6al4v in ultra-precision machining, The International Journal of Advanced Manufacturing Technology 86 (5-8) (2016) 1311–1317.

[41] X. Jin, Y. Altintas, Prediction of micro-milling forces with finite element method, Journal of Materials Processing Technology 212 (3) (2012) 542–552.

[42] J. Lin, J. Han, X. Zhou, Z. Hao, M. Lu, Study on predictive model of cutting force and geometry parameters for oblique elliptical vibration cutting, International Journal of Mechanical Sciences 117 (2016) 43–52.

[43] Z. Zhu, S. To, W.-L. Zhu, P. Huang, Feasibility study of the novel quasi-elliptical tool servo for vibration suppression in the turning of micro-lens arrays, International Journal of Machine Tools and Manufacture 122 (2017) 98 – 105.

[44] J. Manjunathaiah, W. Endres, A study of apparent negative rake angle and its effect on shear angle during orthogonal cutting with edge-radiused tools, Transactions of NAMRI/SME (2000) 197–202.

[45] N. K. Chandiramani, T. Pothala, Dynamics of 2-dof regenerative chatter during turning, Journal of sound and vibration 290 (1) (2006) 448–464.

[46] J. Lin, C. Weng, Nonlinear dynamics of the cutting process, International Journal of Mechanical Sciences 33 (8) (1991) 645–657.

[47] G. Ye, S. Xue, M. Jiang, X. Tong, L. Dai, Modeling periodic adiabatic shear band evolution during high speed machining ti-6al-4v alloy, International journal of plasticity 40 (2013) 39–55.

[48] T. J. Burns, M. A. Davies, Nonlinear dynamics model for chip segmentation in machining, Physical Review Letters 79 (3) (1997) 447.

[49] X. Zhang, Q. Liu, X. Zhou, C. Lin, Determining issues in optimal turning of micro-structured functional surfaces, The International Journal of Advanced Manufacturing Technology 81 (1-4) (2015) 387–396.

[50] M. Shatla, C. Kerk, T. Altan, Process modeling in machining. part i: determination of flow stress data, International Journal of Machine Tools and Manufacture 41 (10) (2001) 1511–1534.

[51] A. Toropov, S.-L. Ko, Prediction of tool-chip contact length using a new slip-line solution for orthogonal cutting, International Journal of Machine Tools and Manufacture 43 (12) (2003) 1209–1215.

[52] M. Malekian, S. S. Park, M. B. Jun, Modeling of dynamic micro-milling cutting forces, International Journal of Machine Tools and Manufacture 49 (7) (2009) 586–598.

[53] J. H. Ko, Time domain prediction of milling stability according to cross edge radiuses and flank edge profiles, International Journal of Machine Tools and Manufacture 89 (2015) 74–85.

[54] D. Germain, G. Fromentin, G. Poulachon, S. Bissey-Breton, From large-scale to micromachining: A review of force prediction models, Journal of Manufacturing Processes 15 (3) (2013) 389–401.

List of Figures

Figure 12 Characteristics of the practical and estimated main cutting force, (a) the cutting force in one revolution of the spindle, and (b) an enlarged view of the forces from 1.5 s to 3 s.

Figure 13 Modeling error of the main cutting force.

Figure 14 Characteristics of the practical and estimated thrust force.

List of Tables